

# **Supporting Information:**

## **Decoding the Competing Effects of Dynamic Solvation Structures on Nuclear Magnetic Resonance Chemical Shifts of Battery Electrolytes via Machine Learning**

Qi You<sup>#,†</sup> Yan Sun<sup>#,†,‡</sup> Feng Wang,<sup>¶</sup> Jun Cheng,<sup>\*,†,¶,§</sup> and Fujie Tang<sup>\*,||,¶,§</sup>

<sup>†</sup>*State Key Laboratory of Physical Chemistry of Solid Surface, iChEM, College of Chemistry and Chemical Engineering, Xiamen University, Xiamen, 361005, China*

<sup>‡</sup>*State Key Laboratory of Catalysis, iChEM, Dalian Institute of Chemical Physics, Chinese Academy of Sciences, Dalian, 116023, China.*

<sup>¶</sup>*Laboratory of AI for Electrochemistry (AI4EC), Tan Kah Kee Innovation Laboratory (IKKEM), Xiamen, 361005, China*

<sup>§</sup>*Institute of Artificial Intelligence, Xiamen University, Xiamen, 361005, China*

<sup>||</sup>*Pen-Tung Sah Institute of Micro-Nano Science and Technology, Xiamen University, Xiamen, 361005, China*

E-mail: chengjun@xmu.edu.cn; tangfujie@xmu.edu.cn

## **Contents**

|   |            |
|---|------------|
| <b>1 Pre-equilibrium of Initial Structures and Machine Learning Molecular Dynamics (MLMD) Simulations</b> | <b>S-2</b> |
|---|------------|

|                   |   |             |
|-------------------|---|-------------|
| <b>2</b>          | <b>Ab-intio Molecular Dynamics (AIMD) for 4 M LiFSI/DME Electrolytes</b>  | <b>S-3</b>  |
| <b>3</b>          | <b>NMR Computational Setup</b>  | <b>S-5</b>  |
| <b>4</b>          | <b>Distance Cutoff Test for Determining the Number of Solvation Shells</b>                                      | <b>S-8</b>  |
| <b>5</b>          | <b>Structural Descriptor Parameters</b>   | <b>S-9</b>  |
| <b>6</b>          | <b>Details of Neural Network (NN) Architecture and Validation of NMR Prediction NN Model</b>                    | <b>S-10</b> |
| <b>7</b>          | <b>Local Structure Index (LSI) Definition</b>   | <b>S-10</b> |
| <b>8</b>          | <b>Assignment of Principal Component Analysis (PCA) for Li<sup>+</sup> Solvation Structural Pattern Mapping</b> | <b>S-12</b> |
| <b>9</b>          | <b>Electron Localization Function (ELF)</b>   | <b>S-14</b> |
| <b>10</b>         | <b>Phase Separation of DME and FSI<sup>-</sup></b>  | <b>S-14</b> |
| <b>11</b>         | <b>Computational Cost of Machine Learning Methods</b>   | <b>S-16</b> |
| <b>References</b> |   | <b>S-16</b> |

## **1 Pre-equilibrium of Initial Structures and Machine Learning Molecular Dynamics (MLMD) Simulations**

The Molecular Dynamics simulations mentioned in this section are all performed with the Large-scale Atomic/Molecular Massively Parallel Simulator (LAMMPS) package.<sup>S1</sup> Initial configurations are constructed with the PACKMOL package<sup>S2</sup> and then pre-equilibrated through OPLS/AA force field,<sup>S3</sup> the parameters of which are generated by LigParGen web server.<sup>S4</sup> For the pre-equilibrated process, we first apply the NVT ensemble for 500 ps and

then use the NPT ensemble with a pressure of 1 bar for 2 ns, both of which are performed at 300 K. Based on the average simulation box sizes and their corresponding snapshots obtained from NPT ensemble, Tab. S1 presents the compositions of LiFSI/DME, and the cell sizes for four salt concentrations. After that, the NVT ensemble is applied at 300 K for 10 ns for each concentration through MLMD simulations. The Nose-Hoover thermostat is employed to generate the NVT ensembles. The average chemical shifts predicted by the NN model for each concentration can be seen in Fig. S2. The radial distribution functions (RDFs) from MLMD simulations of aqueous electrolytes at various concentrations are shown in Fig. S3.

The Machine Learning Potentials (MLPs) mentioned above are generated in deep potential smooth edition (DeePMD-SE) kit.<sup>S5,S6</sup> The root-mean-squared-error (RMSE) of the MLP predictions on the validation dataset is  $\sim 2.50$  meV/atom for potential energies,  $\sim 114.29$  meV/ $\text{\AA}$  for atomic forces, and  $\sim 2.67$  meV/atom for virial stresses (Fig.S1, demonstrating sufficient accuracy to reproduce AIMD trajectories. The DFT-labeled datasets are implemented in CP2K/QUICKSTEP package.<sup>S7</sup> The density functional implementation is based on the hybrid Gaussian plane wave scheme, and the cutoff energy of the finest grid level of plane wave density was set to 900 Ry. The Perdew-Burke-Ernzerhof (PBE) functional<sup>S8</sup> is used to describe the exchange-correlation effect with the Grimme D3<sup>S9</sup> method for van der Waals correction (PBE-D3). All atoms are treated with Goedecker-Teter-Hutter (GTH) pseudopotentials.<sup>S10,S11</sup> The DZVP-MOLOPT-SR-GTH Gaussian basis set is employed for all atom types.<sup>S12</sup> Further details about the training, exploring and labeling process can be found in previous publications from our group.<sup>S13-S15</sup>

## 2 Ab-intio Molecular Dynamics (AIMD) for 4 M LiFSI/DME Electrolytes

To validate the accuracy of MLPs, we perform AIMD simulations for 4 M case. The pre-equilibrium process has been introduced in the previous section. After obtaining the suitable

Table S1: Composition of LiFSI/DME solutions

| Concentration (M) | Number of DME | Number of LiFSI | Box Size (Å) |
|-------------------|---------------|-----------------|--------------|
| 0.97              | 10            | 85              | 25.803       |
| 2.25              | 23            | 75              | 25.706       |
| 3.28              | 34            | 70              | 25.821       |
| 4.19              | 45            | 66              | 26.120       |

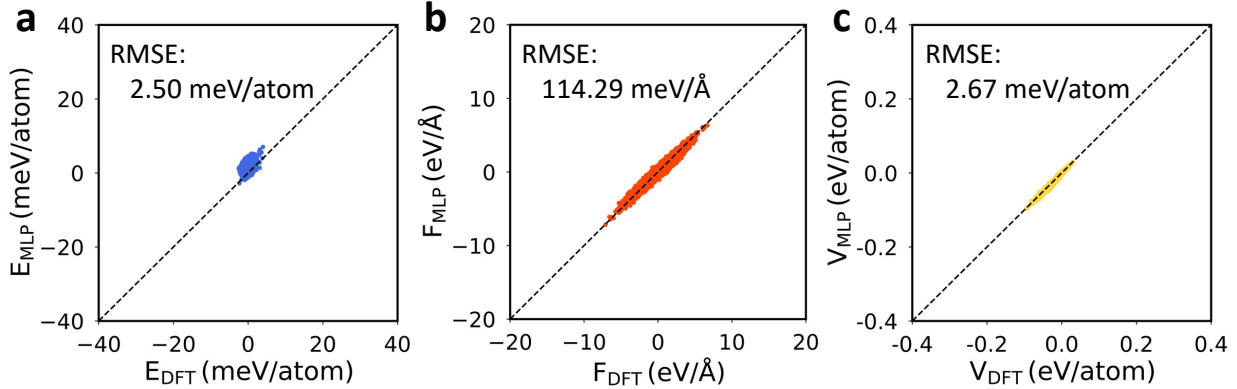


Figure S1: Errors in (a) potential energies, (b) atomic forces and (c) virial stresses predicted by MLPs model on validation datasets. Root-mean-squared-errors (RMSEs) are shown in the inset of the figure.

cell size of the 4 M LiFSI/DME, we conduct 6 ns Classical MD using the NVT ensemble and then sparsely extract 10 structures with the same interval. For each AIMD simulation, we take  $\sim 5$  ps as preliminary equilibration, which is followed by  $\sim 20$  ps of AIMD. At the same time, we produce 20 ps MLMD simulation trajectories using the given 10 balanced structures from AIMD simulations. The radial distribution function (RDF) comparisons between AIMD and MLMD simulations are depicted in Fig. S4. The similar peak positions and line shapes reveal that the MLP performs well in describing the atomic interactions, either the  $\text{Li}^+ \text{-Li}^+$  or  $\text{Li}^+ \text{-O}$  atoms.

AIMD simulations are performed in CP2K/QUICKSTEP package.<sup>S7</sup> We set the cutoff energy of the finest grid level of plane wave density to 400 Ry. The PBE functional<sup>S8</sup> is used to describe the exchange-correlation effect with the Grimme D3<sup>S9</sup> method for disper-

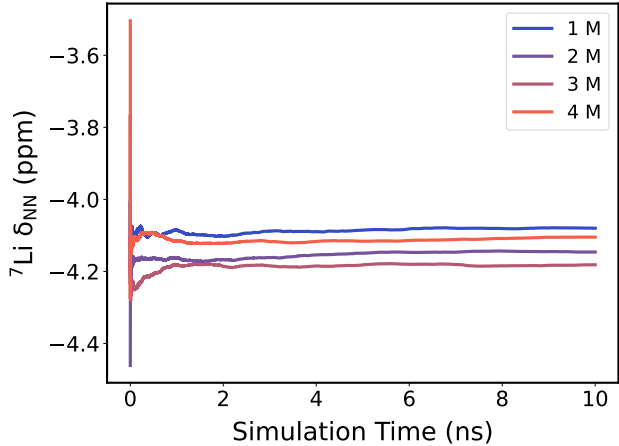


Figure S2: The averaged  ${}^7\text{Li} \delta_{NN}$  of 1-4 M LiFSI/DME electrolytes with the simulation time, using 10 ns MLMD simulation trajectories.

sion correction (PBE-D3). All atoms are treated with GTH pseudopotentials<sup>S10,S11</sup> and the DZVP-MOLOPT-SR-GTH Gaussian basis set.<sup>S12</sup> The AIMD simulations are accomplished in the canonical ensemble (NVT) with a timestep of 0.5 fs and a target temperature of 300 K.

### 3 NMR Computational Setup

All DFT calculations for NMR are performed in Gaussian 16.<sup>S16</sup> NMR calculations for clusters are conducted at the revTPSS<sup>S17,S18</sup>/pcSseg-1<sup>S19</sup> level using the polarizable continuum model (PCM) solvation model to describe the dielectric continuum outside the solute cavity.<sup>S20</sup> For the solvent parameters definition, we set the static dielectric constant Eps as 7.41 for 1,2-Dimethoxyethane (DME) solvents at 293.15 K, the parameter of which is obtained from CRC handbook of chemistry and physics.<sup>S21</sup> Then we acquire the isotropic shielding values from outputs, which need to be converted into the chemical shift referenced to the experiment by using the formula below:

$$\delta[\text{ppm}] = \sigma_{\text{ref}} - \sigma_{\text{iso}} \quad (1)$$

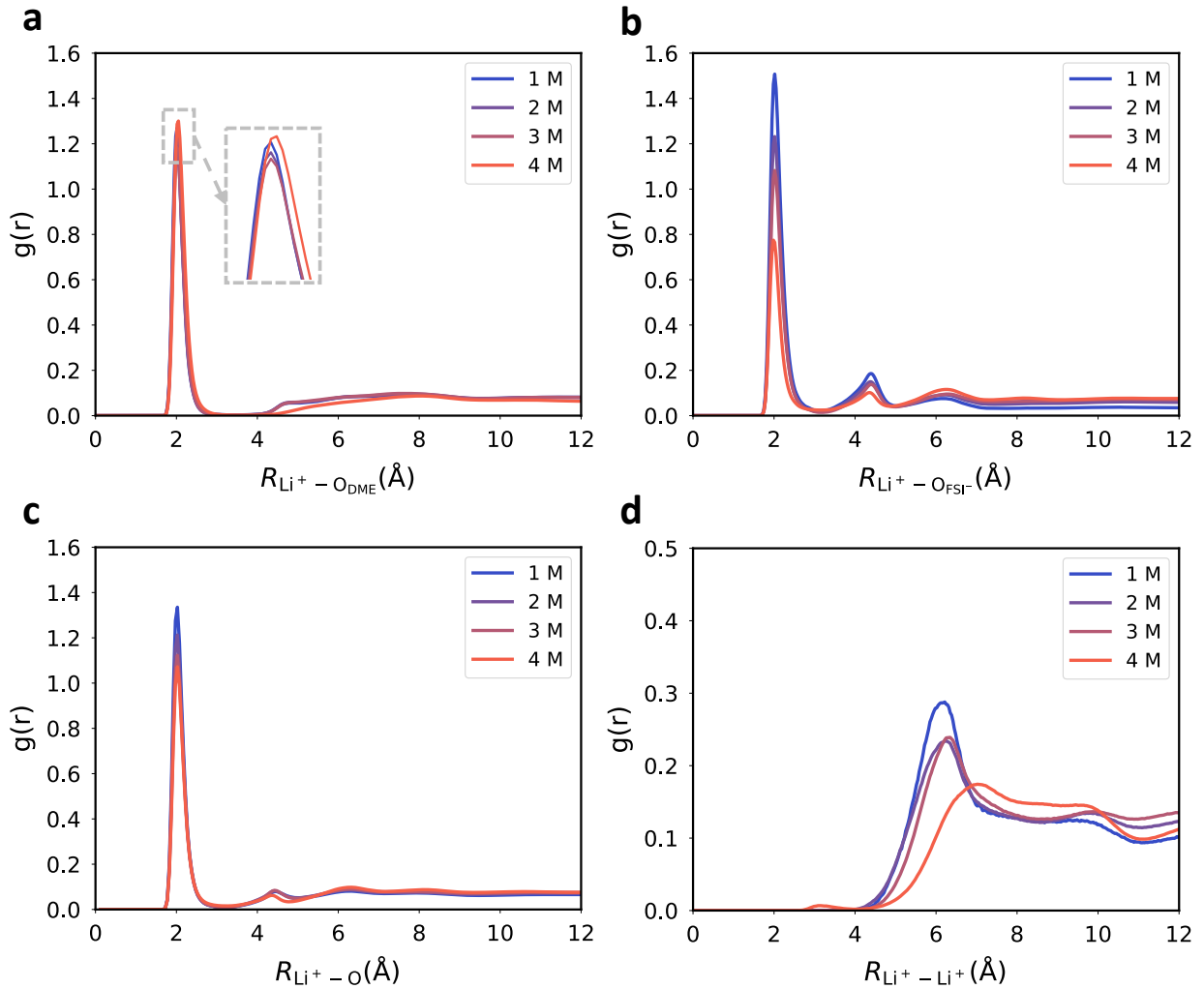


Figure S3: Radial distribution functions (RDFs) for (a)  $\text{Li}^+$  to O atoms of DME molecules, (b)  $\text{Li}^+$  to O atoms of  $\text{FSI}^-$  anions, (c)  $\text{Li}^+$  to all O atoms and (d)  $\text{Li}^+$  to  $\text{Li}^+$  ions for different LiFSI concentration trajectories generated in MLMD simulations.

where  $\sigma_{\text{iso}}$  and  $\delta$  are the isotropic shielding value and the chemical shift of the particular nucleus. Since we focus on the trend across concentrations, the averaged chemical shift for the lowest concentration electrolyte has been aligned to the same experimental value of  $-4.08$  ppm. That is, the chemical reference  $\sigma_{\text{ref}}$  is the sum of the averaged isotropic shielding constant and the experimental chemical shift, both are given from the 1 M case. The chemical shifts for the other three concentrations have been corrected according to the difference  $\sigma_{\text{ref}}$ .

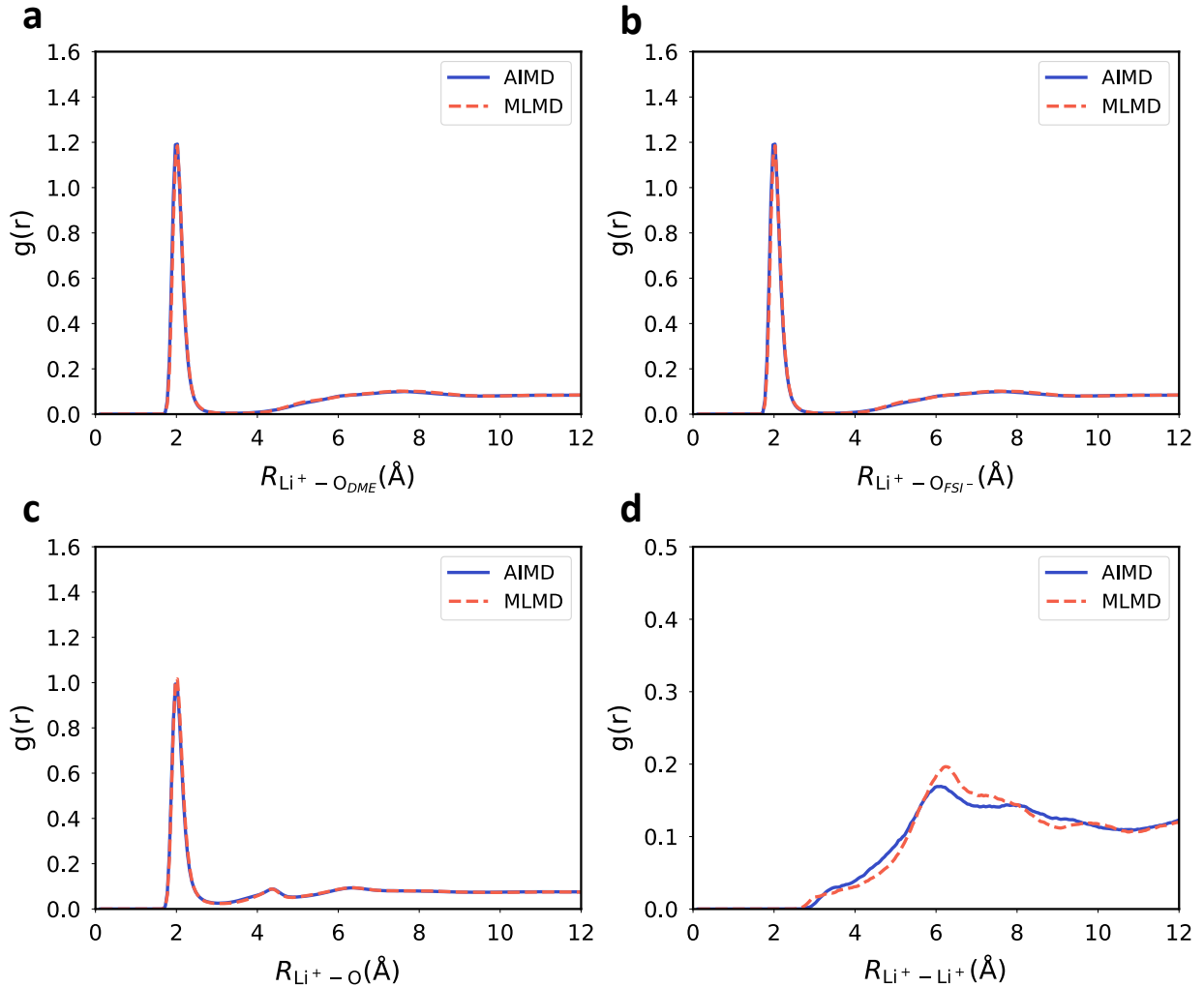


Figure S4: Comparisons of RDFs between AIMD and MLMD simulations for 4 M LiFSI/DME solution. RDFs for (a)  $\text{Li}^+$  to O atoms of DME molecules, (b)  $\text{Li}^+$  to O atoms of  $\text{FSI}^-$  anions, (c)  $\text{Li}^+$  to all O atoms and (d)  $\text{Li}^+$  to  $\text{Li}^+$  ions. The slight difference between AIMD and MLMD may be caused by the difference in the DFT setup used in AIMD and the data for MLP training.

## 4 Distance Cutoff Test for Determining the Number of Solvation Shells

We perform a distance cutoff test for NMR calculations by extracting clusters under three conditions: (i) including only the first solvation shell, (ii) truncated at the second solvation shell, and (iii) encompassing the third solvation shell. Molecules with atoms within cutoff radii of 3.0 Å, 5.0 Å, and 7.0 Å from Li<sup>+</sup> are included to preserve the integrity of the solvation structure, corresponding to the first, second, and third minima of the Li–O RDF in Fig. S3(c). For each concentration, we sample clusters at consistent intervals and computed <sup>7</sup>Li NMR chemical shifts across different solvation shell ranges, yielding approximately 300 chemical shift values per shell range. The trends observed in Fig. S5 show that the chemical shift variations follow the same direction across all three solvation shell ranges, indicating that using only the first solvation shell around a given Li<sup>+</sup> is a practical and reliable approach.

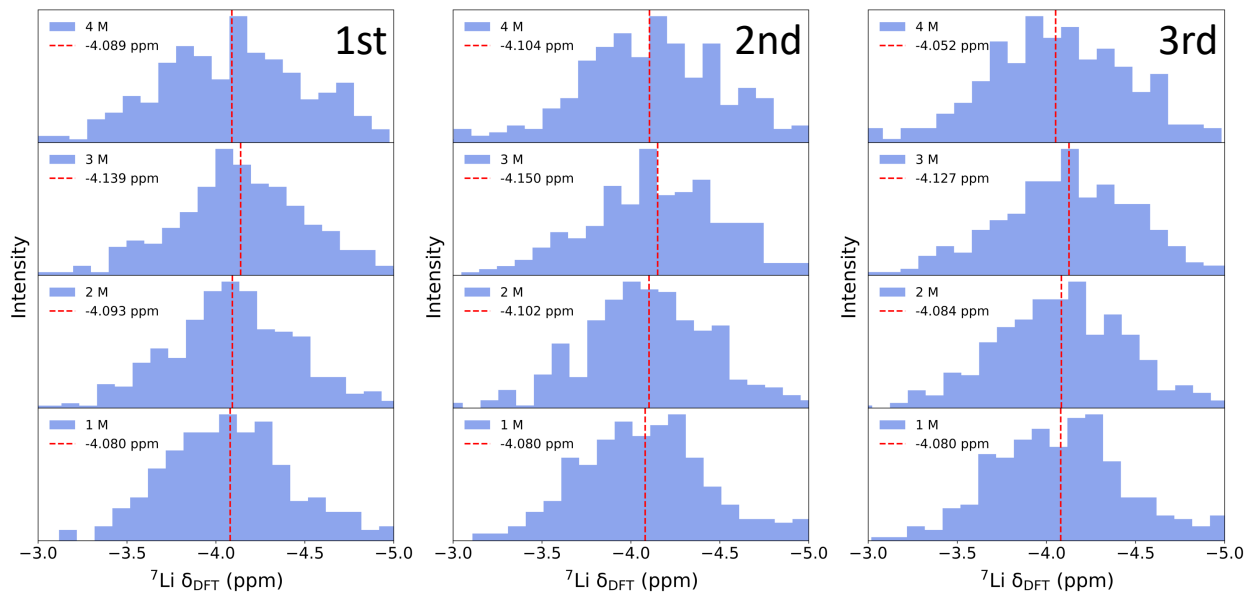


Figure S5: <sup>7</sup>Li NMR chemical shifts for four concentrations, considering distance cutoffs from the central atoms: (a) 3.0 Å, (b) 5.0 Å, and (c) 7.0 Å. These distances correspond to the first, second, and third solvation shells. The chemical shift trends remain consistent across all three distances.

## 5 Structural Descriptor Parameters

We utilize the Local Many-body Tensor Representation (LMBTR)<sup>S22</sup> descriptor to encode the structures, which is a modification of the Many-body Tensor Representation (MBTR) descriptor for local environments. The general MBTR equation is as follows:

$$f_k(x, z) = \sum_{i=1}^{N_a} w_k(i) D(x, g_k(x)) \prod_{j=1}^k C_{z_j, z_{ij}} \quad (2)$$

where  $N_a$  is the number of atoms located within the cutoff radius from the central atom, and index  $i$  refers to one specific atom among the  $N_a$  atoms,  $D$  is broadened probabilistic distribution, and  $g_k$  is a geometric function for k-body terms. In this work, we employ  $g_2$  for the distance of paired atoms and  $g_3$  for the angles among every three atoms, the scalar values of which are both broadened by Gaussian kernel through Dscribe package.<sup>S23</sup> The exponential weight functions for  $g_2$  and  $g_3$  respectively are:

$$w_2^{l,m} = e^{-s_k|R_l - R_m|} \quad (3)$$

$$w_3^{l,m,n} = e^{-s_k(|R_l - R_m| + |R_m - R_n| + |R_l - R_n|)} \quad (4)$$

where  $s_k$  is to set the smoothness cutoff. All related parameters are listed in Tab. S2.

Table S2: LMBTR parameters

| function | grid     |     |     |       | weighting |       |           |
|----------|----------|-----|-----|-------|-----------|-------|-----------|
|          | min      | max | n   | sigma | function  | scale | threshold |
| k2       | distance | 0   | 6   | 200   | 0.1       | exp   | 0.5       |
| k3       | distance | 0   | 180 | 200   | 0.1       | exp   | 0.5       |

## 6 Details of Neural Network (NN) Architecture and Validation of NMR Prediction NN Model

The NN prediction model is initialized and trained in PyTorch.<sup>S24</sup> The NN architecture consists of three fully connected layers, each with 256 nodes, applying affine linear transformations to the input data. The rectified linear unit (ReLU) function is applied after the first two layers to introduce non-linearity. Besides, the mean squared error (MSE) function is applied to track model performance compared with the actual outcomes, guiding the optimization of model parameters during the training process. The details of hyperparameters are listed in Tab. S3. We split the NMR dataset into an 8:1:1 ratio, corresponding to the training, testing, and validation dataset. The accuracy of the NN model is illustrated in Fig. S6, with the RMSE being approximately 0.13 ppm.

Table S3: Neural network parameters

| Hyperparameters        | Value         |
|------------------------|---------------|
| Learning rate          | 0.001         |
| Epochs                 | 1000          |
| Hidden layers          | 3             |
| Nodes of hidden layers | (256,256,256) |
| Activation function    | ReLU          |
| Optimizer              | Adam          |

## 7 Local Structure Index (LSI) Definition

The Local Structure Index (LSI) parameter is the mean-squared-deviation among the radial distances between a given  $\text{Li}^+$  ion and the surrounding oxygen atoms, which quantifies the inhomogeneity in the radial distance distribution.<sup>S25–S27</sup> Here, we set a cutoff distance of 3.0 Å from a given  $\text{Li}^+$  to its surrounding oxygen atoms. Assume there are N oxygen atoms,

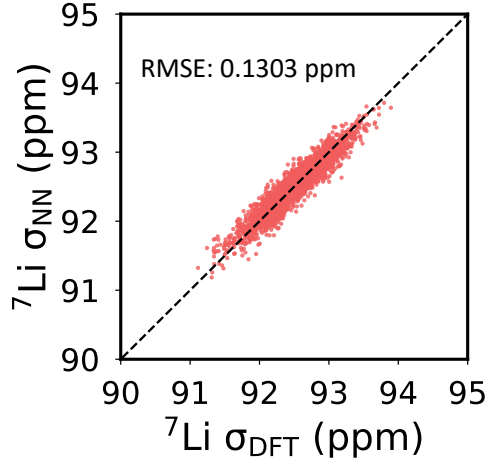


Figure S6: Errors in isotropic shielding values ( $\sigma$ ) by NN model on validation data sets. RMSE is shown in the inset of the figure.

each at a distance  $r_j$  within 3.0 Å from a given  $\text{Li}^+$  ion, arranged in the following order:  $r_1 < r_2 < r_3 < \dots < r_j < r_{j+1} < \dots < r_N < 3.0 \text{ \AA} < r_{N+1}$ . The LSI value is calculated in the following formula:

$$\text{LSI} = \frac{1}{N} \sum_{j=1}^N [\Delta_{j+1,j} - \langle \Delta \rangle]^2 \quad (5)$$

$$\Delta_{j+1,j} \equiv r_{j+1} - r_j \quad (6)$$

where  $\langle \Delta \rangle$  is the mean value of  $\Delta_{j+1,j}$ . Since the situation in the electrolyte is different from that in the pure water, the O atoms beyond the cut may be too far apart, making them irrelevant to the packing density of the shell. Therefore, we modify the consideration of  $r_{N+1}$  by fixing it to the smallest value among all possible  $r_{N+1}$  for each snapshot. When the LSI value is high, there is an obvious separation between the first and second coordination shells. Whereas, if the LSI value is low, the environment surrounding the particular  $\text{Li}^+$  ion is more disordered. This indicates the ambiguous interstitial region between two coordination shells, into which neighboring oxygen atoms have entered. Through the LSI analysis, we find the high coordination number configurations ( $n_{\text{FSI}^-} \geq 4$ ) form extended  $\text{Li}^+-\text{FSI}^-$  chain clusters,

with  $n_{\text{FSI}^-} = 1$  clusters appearing along the boundaries of with these AGG<sup>+</sup>-like structures at 4 M.

## 8 Assignment of Principal Component Analysis (PCA) for Li<sup>+</sup> Solvation Structural Pattern Mapping

We have demonstrated the PCA mapping for Li<sup>+</sup> local environments across all the concentrations in the main text, the exact mappings for every concentration are also illustrated in Fig. S7. We tabulate the detailed assignment for each colored region in Tab. S4, showing prior types of solvation structures corresponding to each region.

Table S4: The solvation structures assignment for different colored regions

| Concentration (M) | 1 M                    | 2 M   | 3 M   | 4 M   |
|-------------------|------------------------|---|---|---|
| Blue              | $n_{\text{FSI}^-} = 3$ | $n_{\text{FSI}^-} = 3$                      | $n_{\text{FSI}^-} = 3/n_{\text{FSI}^-} = 4$ | $n_{\text{FSI}^-} = 3/n_{\text{FSI}^-} = 4$ |
| Green             | $n_{\text{FSI}^-} = 2$ | $n_{\text{FSI}^-} = 2/n_{\text{FSI}^-} = 3$ | $n_{\text{FSI}^-} = 2/n_{\text{FSI}^-} = 3$ | $n_{\text{FSI}^-} = 2/n_{\text{FSI}^-} = 3$ |
| Yellow            | $n_{\text{FSI}^-} = 1$ | $n_{\text{FSI}^-} = 1$                      | $n_{\text{FSI}^-} = 1$                      | $n_{\text{FSI}^-} = 1$                      |
| Red               | $n_{\text{FSI}^-} = 0$ | $n_{\text{FSI}^-} = 0$                      | $n_{\text{FSI}^-} = 0$                      | $n_{\text{FSI}^-} = 0$                      |

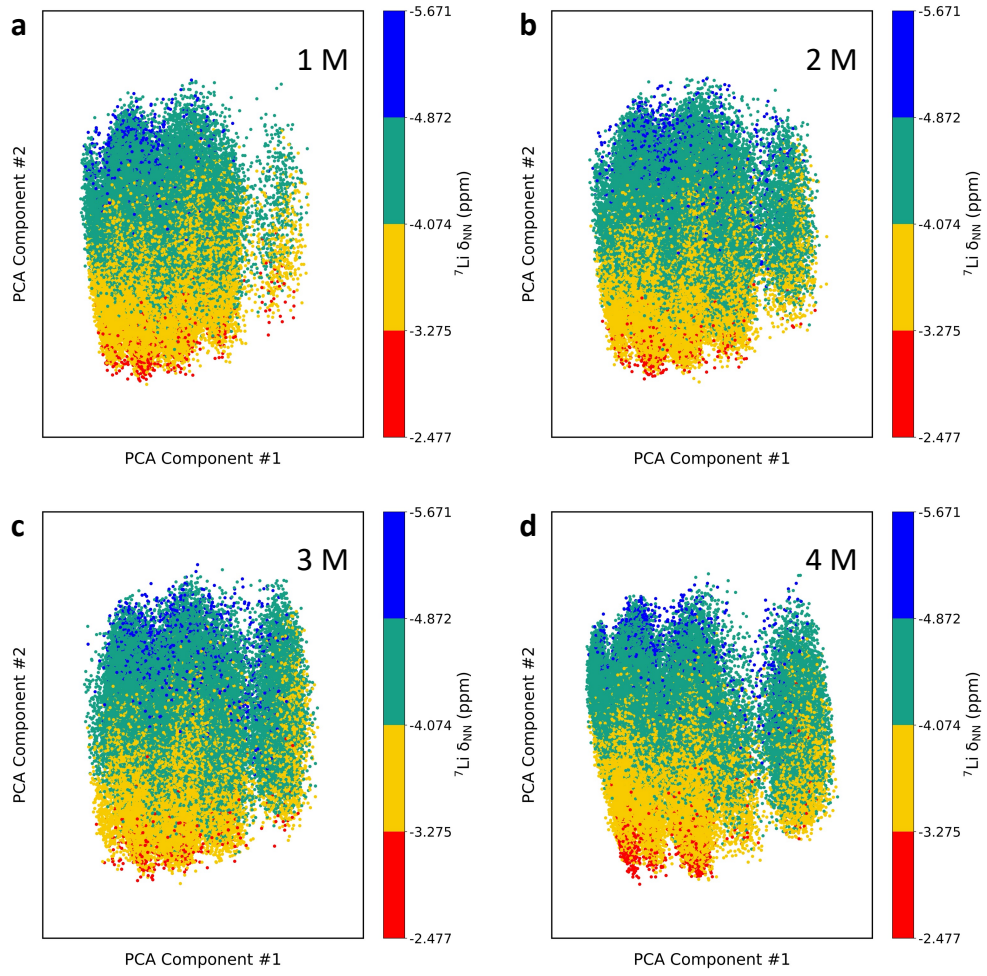


Figure S7: The detailed decomposition of PCA for  $\text{Li}^+$  solvation structural pattern mapping at 1-4 M concentrations, respectively.

## 9 Electron Localization Function (ELF)

The Electron Localization Function (ELF) of the Li nucleus is obtained by the Multiwfn package<sup>S28,S29</sup> and ChimeraX.<sup>S30</sup> To quantify the deformation, we extract the ELF surface area  $A_{\text{ELF}}$  and the ELF volume  $V_{\text{ELF}}$  around the Li nucleus at an isovalue of 0.5. The deformation factor is defined as:

$$\phi = \frac{A_{\text{ELF}}}{A_{\text{Sphere}}} \quad (7)$$

where  $A_{\text{Sphere}}$  represents the surface area of a sphere whose volume is the same as  $V_{\text{ELF}}$ .<sup>S31</sup>

## 10 Phase Separation of DME and FSI<sup>-</sup>

We analyze the distribution of molecules near the central Li<sup>+</sup> ions under the four concentrations, taking the midpoint of the molecules as a reference. As shown in Fig. S8, the spatial distribution of DME (blue) and FSI<sup>-</sup> (red) is presented within a shell of radius 3 Å, centered around the Li<sup>+</sup> ions (pink). It is evident that more FSI<sup>-</sup> anions aggregate in the first solvation shell at 4 M concentration.

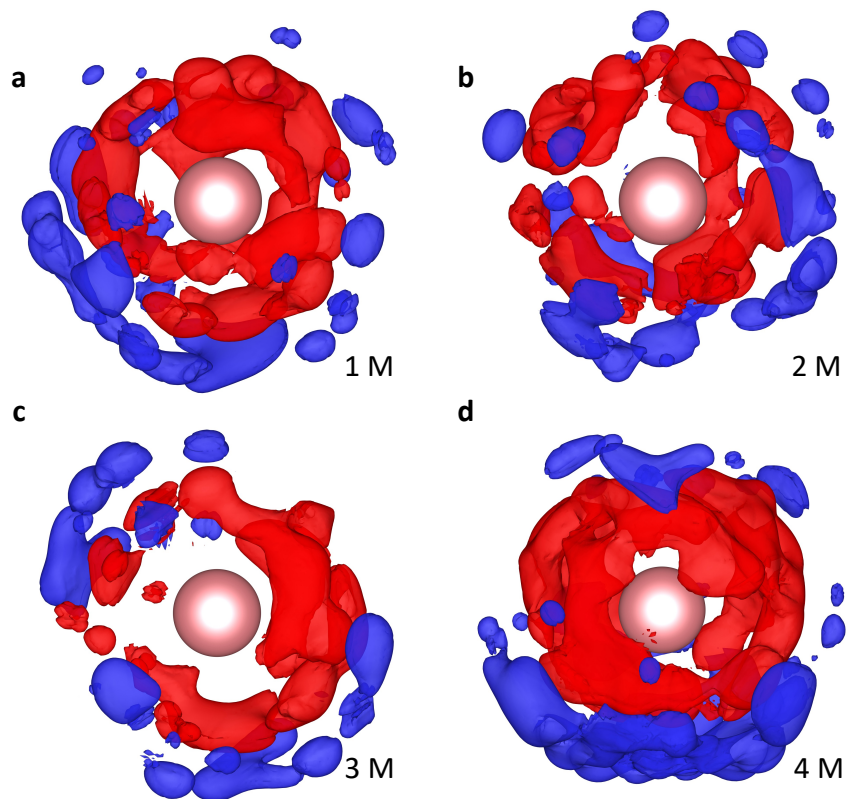


Figure S8: Schematic diagram of DME (blue) and  $\text{FSI}^-$  (red) spatial distribution for (a) 1 M, (b) 2 M, (c) 3 M, and (d) 4 M within the 3  $\text{\AA}$  around the given  $\text{Li}^+$  ion (pink), indicating that more  $\text{FSI}^-$  anions aggregate near the  $\text{Li}^+$  ion at 4 M. The isosurface at a density of  $0.002 \text{ \AA}^{-3}$  and the distribution is analyzed using the midpoint of the molecules as a reference.

## 11 Computational Cost of Machine Learning Methods

Tab. S5 summarizes the computational cost of MLMD simulations, NN training, and NMR calculations. MLMD simulations are performed on an Nvidia A100 80GB SXM GPU, requiring 21 hours to simulate a 1,500-atom system for 10 ns with a timestep of 0.5 fs. NN training is conducted on the same hardware and completed in 1 hour for a dataset of 30,000  $^7\text{Li}$  chemical shifts. NMR calculations are carried out on an Intel 6338 Xeon CPU, with the number of atoms and their corresponding computational times also listed in Tab. S5. Notably, when the number of atoms exceeds 200, the computational cost time increases disproportionately (non-linearly). These results highlight the feasibility of our approach in terms of computational efficiency.

Table S5: Computational cost

| Task                    | Device                             | Scale                                | Time   |
|-------------------------|------------------------------------|--------------------------------------|--------|
| MLMD Simulation (10 ns) | 1 * Nvidia A100 80GB SXM GPU       | 1,500 atoms                          | 21 h   |
| NN Training             | 1 * Nvidia A100 80GB SXM GPU       | 30,000 $^7\text{Li}$ chemical shifts | 1 h    |
|                         |                                    | 50 atoms                             | 4 min  |
|                         |                                    | 100 atoms                            | 10 min |
| NMR Calculation         | 2 * Intel 6338 Xeon CPU (32 cores) | 150 atoms                            | 15 min |
|                         |                                    | 200 atoms                            | 20 min |
|                         |                                    | 250 atoms                            | 50 min |
|                         |                                    | 300 atoms                            | 1 h    |

## References

- (S1) Thompson, A. P.; Aktulga, H. M.; Berger, R.; Bolintineanu, D. S.; Brown, W. M.; Crozier, P. S.; in 't Veld, P. J.; Kohlmeyer, A.; Moore, S. G.; Nguyen, T. D.; Shan, R.; Stevens, M. J.; Tranchida, J.; Trott, C.; Plimpton, S. J. LAMMPS - a flexible simu-

lation tool for particle-based materials modeling at the atomic, meso, and continuum scales. *Comput. Phys. Commun.* **2022**, 271, 108171.

- (S2) Martínez, L.; Andrade, R.; Birgin, E. G.; Martínez, J. M. PACKMOL: A package for building initial configurations for molecular dynamics simulations. *J. Comput. Chem.* **2009**, 30, 2157–2164.
- (S3) Robertson, M. J.; Tirado-Rives, J.; Jorgensen, W. L. Improved Peptide and Protein Torsional Energetics with the OPLS-AA Force Field. *J. Chem. Theory Comput.* **2015**, 11, 3499–3509.
- (S4) Dodda, L. S.; Cabeza de Vaca, I.; Tirado-Rives, J.; Jorgensen, W. L. LigParGen web server: an automatic OPLS-AA parameter generator for organic ligands. *Nucleic Acids Res.* **2017**, 45, W331–W336.
- (S5) Zhang, L.; Han, J.; Wang, H.; Car, R.; E, W. Deep Potential Molecular Dynamics: A Scalable Model with the Accuracy of Quantum Mechanics. *Phys. Rev. Lett.* **2018**, 120, 143001.
- (S6) Zhang, L.; Han, J.; Wang, H.; Car, R.; E, W. Deep Potential Molecular Dynamics: A Scalable Model with the Accuracy of Quantum Mechanics. *Phys. Rev. Lett.* **2018**, 120, 143001.
- (S7) VandeVondele, J.; Krack, M.; Mohamed, F.; Parrinello, M.; Chassaing, T.; Hutter, J. Quickstep: Fast and accurate density functional calculations using a mixed Gaussian and plane waves approach. *Comput. Phys. Commun.* **2005**, 167, 103–128.
- (S8) Perdew, J. P.; Burke, K.; Ernzerhof, M. Generalized Gradient Approximation Made Simple. *Phys. Rev. Lett.* **1996**, 77, 3865–3868.
- (S9) Grimme, S.; Antony, J.; Ehrlich, S.; Krieg, H. A consistent and accurate ab initio

parametrization of density functional dispersion correction (DFT-D) for the 94 elements H-Pu. *J. Chem. Phys.* **2010**, 132, 154104.

- (S10) Hartwigsen, C.; Goedecker, S.; Hutter, J. Relativistic separable dual-space Gaussian pseudopotentials from H to Rn. *Phys. Rev. B* **1998**, 58, 3641–3662.
- (S11) Goedecker, S.; Teter, M.; Hutter, J. Separable dual-space Gaussian pseudopotentials. *Phys. Rev. B* **1996**, 54, 1703–1710.
- (S12) VandeVondele, J.; Hutter, J. Gaussian basis sets for accurate calculations on molecular systems in gas and condensed phases. *J. Chem. Phys.* **2007**, 127, 114105.
- (S13) Wang, F.; Sun, Y.; Cheng, J. Switching of Redox Levels Leads to High Reductive Stability in Water-in-Salt Electrolytes. *J. Am. Chem. Soc.* **2023**, 145, 4056–4064.
- (S14) Wang, F.; Ma, Z.; Cheng, J. Accelerating Computation of Acidity Constants and Redox Potentials for Aqueous Organic Redox Flow Batteries by Machine Learning Potential-Based Molecular Dynamics. *J. Am. Chem. Soc.* **2024**, 146, 14566–14575.
- (S15) Wang, F.; Tang, Y.-H.; Ma, Z.-B.; Jin, Y.-C.; Cheng, J. Soaring Chemical Space of Battery Electrolytes Using Universal Machine Learning Potential. 2025; <https://chemrxiv.org/engage/chemrxiv/article-details/67c179776dde43c908d6fedc>.
- (S16) Frisch, M. J.; Trucks, G. W.; Schlegel, H. B.; Scuseria, G. E.; Robb, M. A.; Cheeseman, J. R.; Scalmani, G.; Barone, V.; Petersson, G. A.; Nakatsuji, H.; Li, X.; Caricato, M.; Marenich, A. V.; Bloino, J.; Janesko, B. G.; Gomperts, R.; Mennucci, B.; Hratchian, H. P.; Ortiz, J. V.; Izmaylov, A. F.; Sonnenberg, J. L.; Williams-Young, D.; Ding, F.; Lipparini, F.; Egidi, F.; Goings, J.; Peng, B.; Petrone, A.; Henderson, T.; Ranasinghe, D.; Zakrzewski, V. G.; Gao, J.; Rega, N.; Zheng, G.; Liang, W.; Hada, M.; Ehara, M.; Toyota, K.; Fukuda, R.; Hasegawa, J.; Ishida, M.; Nakajima, T.; Honda, Y.; Kitao, O.; Nakai, H.; Vreven, T.; Throssell, K.; Mont-

gomery, J. A., Jr.; Peralta, J. E.; Ogliaro, F.; Bearpark, M. J.; Heyd, J. J.; Brothers, E. N.; Kudin, K. N.; Staroverov, V. N.; Keith, T. A.; Kobayashi, R.; Normand, J.; Raghavachari, K.; Rendell, A. P.; Burant, J. C.; Iyengar, S. S.; Tomasi, J.; Cossi, M.; Millam, J. M.; Klene, M.; Adamo, C.; Cammi, R.; Ochterski, J. W.; Martin, R. L.; Morokuma, K.; Farkas, O.; Foresman, J. B.; Fox, D. J. Gaussian<sup>TM</sup>16 Revision C.01. 2016; Gaussian Inc. Wallingford CT.

- (S17) Tao, J.; Perdew, J. P.; Staroverov, V. N.; Scuseria, G. E. Climbing the Density Functional Ladder: Nonempirical Meta-Generalized Gradient Approximation Designed for Molecules and Solids. Phys. Rev. Lett. **2003**, 91, 146401.
- (S18) Perdew, J. P.; Ruzsinszky, A.; Csonka, G. I.; Constantin, L. A.; Sun, J. Workhorse Semilocal Density Functional for Condensed Matter Physics and Quantum Chemistry. Phys. Rev. Lett. **2009**, 103, 026403.
- (S19) Jensen, F. Segmented Contracted Basis Sets Optimized for Nuclear Magnetic Shielding. J. Chem. Theory Comput. **2015**, 11, 132–138.
- (S20) Miertuš, S.; Scrocco, E.; Tomasi, J. Electrostatic interaction of a solute with a continuum. A direct utilization of AB initio molecular potentials for the prevision of solvent effects. Chem. Phys. **1981**, 55, 117–129.
- (S21) Haynes, W. M. CRC handbook of chemistry and physics; CRC press, 2016.
- (S22) Huo, H.; Rupp, M. Unified representation of molecules and crystals for machine learning. Mach. Learn.: Sci. Technol. **2022**, 3, 045017.
- (S23) Laakso, J.; Himanen, L.; Homm, H.; Morooka, E. V.; Jäger, M. O.; Todorović, M.; Rinke, P. Updates to the DScribe library: New descriptors and derivatives. J. Chem. Phys. **2023**, 158, 234802.

- (S24) Paszke, A.; Gross, S.; Massa, F.; Lerer, A.; Bradbury, J.; Chanan, G.; Killeen, T.; Lin, Z.; Gimelshein, N.; Antiga, L.; Desmaison, A.; Kopf, A.; Yang, E.; DeVito, Z.; Raison, M.; Tejani, A.; Chilamkurthy, S.; Steiner, B.; Fang, L.; Bai, J.; Chintala, S. *Advances in Neural Information Processing Systems* 32; Curran Associates, Inc., 2019; Vol. 32; pp 8024–8035.
- (S25) Shiratani, E.; Sasai, M. Growth and collapse of structural patterns in the hydrogen bond network in liquid water. *J. Chem. Phys.* **1996**, 104, 7671–7680.
- (S26) Shiratani, E.; Sasai, M. Molecular scale precursor of the liquid–liquid phase transition of water. *J. Chem. Phys.* **1998**, 108, 3264–3276.
- (S27) Biswajit Santra, F. M., Robert A. DiStasio Jr.; Car, R. Local structure analysis in *ab initio* liquid water. *Mol. Phys.* **2015**, 113, 2829–2841.
- (S28) Lu, T.; Chen, F. Multiwfn: A multifunctional wavefunction analyzer. *J. Comput. Chem.* **2012**, 33, 580–592.
- (S29) Lu, T. A comprehensive electron wavefunction analysis toolbox for chemists, Multiwfn. *J. Chem. Phys.* **2024**, 161, 082503.
- (S30) Meng, E. C.; Goddard, T. D.; Pettersen, E. F.; Couch, G. S.; Pearson, Z. J.; Morris, J. H.; Ferrin, T. E. UCSF ChimeraX: Tools for structure building and analysis. *Protein Sci.* **2023**, 32, e4792.
- (S31) Yao, N.; Chen, X.; Sun, S.-Y.; Gao, Y.-C.; Yu, L.; Gao, Y.-B.; Li, W.-L.; Zhang, Q. Identifying the lithium bond and lithium ionic bond in electrolytes. *Chem* **2024**, 11, 102254.